Retrospective Estimation of the Susceptibility Driven Field Map for Distortion Correction in Echo Planar Imaging

Hiroyuki Takeda and Boklye Kim

Department of Radiology, University of Michigan, Ann Arbor, MI, USA
{htakeda,boklyek}@umich.edu

Abstract. Echo planar imaging (EPI) sequence used for acquiring functional MRI (fMRI) time series data provides the advantage of high temporal resolution, but also is highly sensitive to the magnetic field inhomogeneity resulting in geometric distortions. A static field-inhomogeneity map measured before or after the fMRI scan to correct for such distortions does not account for magnetic field changes due to the head motion during the time series acquisition. In practice, the field map dynamically changes with head motion during the scan and leads to variations in the geometric distortion. We model in this work the field inhomogeneity with the object and the scanner dependent terms. The object-specific term varies with the object's magnetic susceptibility and orientation, i.e., head position with respect to B_0. Thus, the simple transformation of the acquired field may not yield an accurate field map. We assume that the scanner-specific field remains unchanged and independent of the head motion. Our approach in this study is to retrospectively estimate the object's magnetic susceptibility (χ) map from an observed high-resolution static field map using an estimator derived from a probability density function of non-uniform noise. This approach is capable of finding the susceptibility map regardless of the wrapping effect. A dynamic field map at each head position can be estimated by applying a rigid body transformation to the estimated χ-map and the 3-D susceptibility voxel convolution (SVC) which is a physics-based discrete convolution model for computing χ-induced field inhomogeneity.

Keywords: Echo planar imaging, geometric distortion correction, field inhomogeneity, susceptibility map.

1 Introduction

While echo planar imaging (EPI) is widely used in functional MRI for brain activation analysis, the measured k-space samples are sensitive to the magnetic field inhomogeneity resulting in geometric distortions of the acquired images [1]. The field map dynamically changes with head motion during the scan, and such changing field map leads considerable variations not only in geometric distortions but also in voxel intensities from one image to another, which negatively impacts the performance of the activation analysis in functional magnetic resonance imaging (fMRI).

J.C. Gee et al. (Eds.): IPMI 2013, LNCS 7917, pp. 352–363, 2013.

Magnetic susceptibility (χ)-induced local field variation due to the human anatomy, mainly the air in the sinus interfaced with tissue and bone, induces the local B0 field inhomogeneity, which is the cause of geometric distortion and signal loss. Such χ–induced local field variation is hard to compensate mechanically by the scanner especially with the presence of motion during fMRI time series acquisitions using the EPI sequence. In practice, the field map dynamically changes with the presence of head motion during the fMRI scan, and such changes lead to variations in geometric distortion. Conventionally, a static field map can be obtained from the phase difference of an image pair acquired at different echo times [2-4]. Approximating a dynamic field map by applying rigid body transformations to an observed static field map may not be sufficient in the presence of significant head rotations with respect to the B0 field since the field inhomogeneity may change nonlinearly [5]. We consider that the acquired field map is comprised of the object-specific, χ-induced, and the system-specific, non-χ-induced components. The χ-induced field inhomogeneity term varies with the object's orientation with respect to B0 while the system-specific field term depends mainly on the bulk changes in the applied static field. For the estimation of a χ-induced field map subject to head rotation at a specific image acquisition time, we first estimate the χ-map from a measured static field map and transform the object-specific χ-map using the estimated the head motion parameters [6-8] and reconstruct a new field map [5, 9] using the susceptibility voxel convolution (SVC) technique [10, 11]. We present in this work the estimation of the χ-induced and non-χ-induced field map, termed system-specific herein, components in human brain data to be used for the computation of dynamic field maps in EPI time series.

The χ-induced field (ΔB_χ) may be the dominant component of the field inhomogeneity changes and approximately expressed as a convolution of the object-specific χ-map with the SVC kernel (h) (i.e., $\Delta B_\chi = B_0 \cdot h * \chi$ where B_0 is the strength of the applied magnetic field) [10, 11]. The previous and commonly used approach for the χ-induced field map estimation is by deconvolution of the measured field map (ΔB) with the SVC kernel [5, 12-27]. Such deconvolution approach in χ-map estimation poses following difficulties:

- The measured field map (ΔB) often suffers from wrapping effects due to large susceptibility value changes in the phase difference $\theta \in (-\pi, \pi]$ between the two complex-valued images acquired at different echo times (T_{E1} and T_{E2}), i.e. $\theta = \frac{1}{\gamma}\Delta B(T_{E2} - T_{E1})$ where γ is the gyromagnetic ratio [28].
- Other than the χ-induced field inhomogeneity, there are other sources of error from the non-χ–induced, system specific magnetic field component [29].
- Noise variance on the acquired phase difference map θ or the local signal-to-noise ratio (SNR) depends on the local signal intensity (i.e., the magnitude of the complex-valued image voxels) causing spatially-varying variance of the noise [30-32].
- The deconvolution process may produce significant ringing/streak artifacts and amplify the phase noise due to the zero fills in the SVC kernel [5, 12-27].

Some of the previous studies on the χ-map estimation employ unwrapping techniques [30-40], and high-pass filtering [18-21, 24, 25, 27, 41] to remove the wrapping effects

and the system-specific inhomogeneous field term, respectively. Then, the weighted least square estimator with an appropriate (smoothing) regularization is used to estimate the χ-map [5, 15-27], where the weights are computed from either the estimation of the local noise variance or local signal magnitudes. Though the potential of the SVC deconvolution approach could be demonstrated, the statistical theory behind the approach is not well utilized in those previous works. Consequently, the performance of the SVC deconvolution approach could not be fully exploited because the unwrapping process may cause additional errors [5, 15-27] or their weighting functions would not quite rely on the property of the noise that the phase data θ carry [5, 15-27]. Some of the methods require masking out the surrounding air region and the skull part of the human head manually in advance, where noise and wrapping effects are severe [16, 19-22, 24-27].

In our work, for the deconvolution approach we take advantage of multiple receiver coils, each of which has non-uniform, complex-valued, sensitivity and provides a separate phase difference map rather than using the combined data. Estimating one χ-map out of multiple datasets is always preferable in terms of SNR. Besides, combining the given phase data from multiple coil channels can introduce additional averaging or combination errors depending on the method used, i.e., sum of squares or Roemer [42].

In this study, in lieu of the previous approaches, we explicitly show appropriate terms in modeling the field homogeneity and an effective probability density function (PDF) of the noise. Using the PDF of the given phase data our estimator penalizes less reliable samples by giving smaller weights for computing the χ-map of the object. Note that, though it was convenient, Gaussian noise does not really represent the noise distribution in the phase domain [30-32], therefore a weighting function is necessary to suppress undesired effects caused by the less reliable phase samples [5, 15-27]. Furthermore, our estimator derived from the PDF is capable of finding a χ-map regardless of phase wrapping effects. Finally, we take into account the scanner-specific, non-χ-induced, field in order to estimate a χ-map accurately [5]. The scanner-specific field component may be identified by scanning a homogeneous head phantom and we introduce regularizations which effectively suppress noise and other artifacts.

This paper is structured as follows. In Section 2, we introduce and derive a χ-map estimator based on our data model and the PDF of the noise ridden on the phase difference map. In Section 3, we show our results from simulation and real MRI scan data, and conclude our paper in Section 4.

2 Susceptibility Map Estimation

A field inhomogeneity map ΔB is obtained from a pair of complex-valued images I_{TE1} and I_{TE2} acquired at different echo times, T_{E1} and T_{E2}, using a dual-echo or multi-echo sequence, by taking the phase difference θ as

$$\theta(\mathbf{r})[\text{rad}] = \angle\{\bar{I}_{TE1}(\mathbf{r}) \cdot I_{TE2}(\mathbf{r})\} = \gamma \Delta B(\mathbf{r}) \Delta T_E - 2\pi n(\mathbf{r}) + \eta(\mathbf{r}) \tag{1}$$

where $\mathbf{r} = [x, y, z, q]$ is the coordinate of the phase difference map, i.e. the 3-D spatial coordinate and the coil channel index, q, γ is the gyromagnetic ratio, $-2\pi n$ represents the wrapping effect with some integer $n(\mathbf{r})$ due to the angle operation and $\theta(\mathbf{r})$ stays in the range of $(-\pi, \pi]$ and $\Delta T_E = T_{E2} - T_{E1}$. The field inhomogeneity map ΔB, model may be comprised of three components: (i) the object's χ-induced field ΔB_χ, which can be computed by the susceptibility voxel convolution (SVC) as $\Delta B_\chi = B_0 \cdot h * \chi$ where h is the three dimensional SVC kernel, (ii) the higher order field perturbation ΔB_e induced by the object's susceptibility and (iii) the system-specific, non-χ-induced, field ΔB_{sys}. We denote the field inhomogeneity map $\Delta B = B_0 \cdot h * \chi + \Delta B_{\text{e}} + \Delta B_{\text{sys}}$ and rewrite the data model (1) as

$$\theta(\mathbf{r}) = \gamma \Delta T_E B_0 \cdot h(\mathbf{r}) * \chi(\mathbf{r}) + \theta_{\text{e}}(\mathbf{r}) + \theta_{\text{sys}}(\mathbf{r}) - 2\pi\, n(\mathbf{r}) + \epsilon(\mathbf{r}), \tag{2}$$

where $\theta_{\text{e}}(\mathbf{r}) = \gamma \Delta T_E \Delta B_{\text{e}}(\mathbf{r})$ and $\theta_{\text{sys}}(\mathbf{r}) = \gamma \Delta T_E \Delta B_{\text{sys}}(\mathbf{r})$. We assume that ΔB_{e} is smooth across the space and ΔB_{sys} is dependent mainly on the system and stays constant for a given magnet system. Modeling and estimating the ΔB_{e} and ΔB_{sys} terms are not like any other existing methods that handle those terms by applying a low-pass filter [19, 41].

Often noise is assumed to be Gaussian and consequently necessitates noise variance estimation for each phase sample prior to the χ-map estimation. However, the multiplication of voxel intensities in the angle operation in the phase map alters the property of the noise carried by the image voxels. In this work, we introduce an approximated probability density function of ϵ. Assuming that the noise ridden on the two images I_{TE1} and I_{TE2} is *i.i.d.* zero-mean complex Gaussian noise with variance of σ^2, where $\sigma^2 \ll var(I_{TE2})$, we can approximately express the PDF of η in (1) as (q.v. Appendix for the derivation),

$$p\big(\eta(\mathbf{r})\big) \propto \exp\{\kappa(\mathbf{r}) \cdot \cos \eta(\mathbf{r})\} \quad \text{where} \quad \kappa(\mathbf{r}) \approx \frac{|I_{TE1}(\mathbf{r})|^2 |I_{TE2}(\mathbf{r})|^2}{(|I_{TE1}(\mathbf{r})|^2 + |I_{TE2}(\mathbf{r})|^2)\sigma^2 + \sigma^4}. \tag{3}$$

It is advantageous that the term $2\pi n$ appeared in (1) has no effect in $\cos(\cdot)$ and the term κ as a weight function, although it is rather related to the reciprocal of the variance of the PDF, eliminates noisy data (i.e. phase samples in the air region and the region where the coil sensitivity is low) by penalizing with small weights.

Having introduced the data model (2) and the noise PDF (3), we have the following maximum likelihood estimator for the χ-map and θ_{e} with regularizations as

$$\max_{\chi, \theta_{\text{e}}} \Big[\sum_{\text{for all } \mathbf{r}} \kappa(\mathbf{r}) \cdot \cos\big\{\theta(\mathbf{r}) - \gamma \Delta T_E B_0 \cdot h(\mathbf{r}) * \chi(\mathbf{r}) - \theta_{\text{e}}(\mathbf{r}) - \tilde{\theta}_{\text{sys}}(\mathbf{r})\big\} - \sum_{i=\{x,y,z\}} \{\mu_1 |\Upsilon_{\text{i}}(\mathbf{r}) * \theta_{\text{e}}(\mathbf{r})|^2 + \mu_2 |\Gamma_i(\mathbf{r}) * \chi(\mathbf{r})|\} \Big], \tag{4}$$

where μ_1 and μ_2 are the regularization parameters for θ_{e} and χ, respectively, and Γ_i and Υ_i are the convolution kernel function of the first and second derivatives, respectively, along i-axis for $i = \{x, y, z\}$. We chose the kernel functions assuming that the secondary field perturbation component θ_{e} is piecewise smooth and the χ-map is piecewise constant across the space. We estimate χ and θ_{e} by the steepest descent method iteratively. We initialize χ by first making a binary image of the body tissue

and air from I_{TE1}. We initialize θ_{e} with residuals, i.e. $\hat{\theta}_{\mathrm{e}}^{(0)} = \theta - \gamma \Delta T_E B_0 \cdot h * \hat{\chi}^{(0)} - \tilde{\theta}_{\mathrm{sys}}$ where $\hat{\chi}^{(0)}$ is the initial χ-map estimate. As for the system-specific component θ_{sys}, we obtain the phase difference map empirically from a pair image of a homogeneous phantom in advance, and smoothen it by the polynomial fitting method for the system-specific component $\tilde{\theta}_{\mathrm{sys}}$.

3 Experiments

Images were acquired from a Philips 3T MRI Ingenia system (Beth, Netherlands). We estimated the system-specific field component $\theta_{\mathrm{sys}} (= \gamma \Delta \mathrm{T_E} \Delta B_{\mathrm{sys}})$ which includes scanner's shimming with a bulk homogeneous object. Using a sphere phantom filled with a homogeneous agar gel (diameter = 22 cm), we empirically estimated θ_{sys}. Using a multiecho sequence, I_{TE1} and I_{TE2} were acquired with $\Delta T_E = 2.0$ ms and image resolution $2 \times 2 \times 2$ mm^3. In Fig 1, the phase image of I_{TE1}, one of the image pair measured from one of the 13 coils (a) and the computed the phase difference map (b) from the pair are shown. Each coil exhibits distinct coil sensitivity and we estimated all data from 13 channels. Also the system-specific field component was explicitly estimated using data from all receiver coils. Assuming that the field is smooth across the space, we estimated $\tilde{\theta}_{\mathrm{sys}}$ with the global polynomial fitting [43] as shown in Fig 1(f). The plots in Fig 2 show the middle cross sections along x, y, z-axes of the acquired phase difference image (circles) and the smoothed phase difference image (solid lines). We assume that the system specific field stays stable for the given MRI scanner [5].

Human brain data were acquired from the same scanner using the same sequence and acquisition parameters as the phantom data. The phase and phase difference images from the first (out of 13) receiver coil are shown in Fig 3(a) and (b), respectively. Fig 3(c) shows the phase difference image after removing the estimated system-specific field, i.e. $\angle(\bar{I}_{TE1} \cdot I_{TE2}) - \tilde{\theta}_{\mathrm{sys}}$ (rad). Using our proposed estimator (4), the χ-map of the human head and ΔB_{e} were estimated as shown in Fig 4 (b) and (c), respectively. We note that the estimated perturbation field ΔB_{e} includes the error caused by the structure of the human head outsides the field of view.

As a comparison, we generated a susceptibility map, χ_{ICBM} by registering a discrete brain atlas data from the International Consortium of Brain Mapping (ICBM) [44] on to the magnitude image of I_{TE1}. The discrete images are segmented into four different parts, air, born, fat, and brain tissues (i.e., white/gray matter, CSF, vessel). Then a theoretical χ-map, χ_{ICBM}, of a human brain was created by filling in the literature susceptibility values to specific segmented structures as shown in Fig 4(a). The susceptibility values $\chi_{\mathrm{air}} = 0.4 \times 10^{-6}$, $\chi_{\mathrm{bone}} = -8.86 \times 10^{-6}$, $\chi_{\mathrm{fat}} = -7.5 \times 10^{-6}$, and $\chi_{\mathrm{tissue}} = -9.05 \times 10^{-6}$ were used [11, 45]. . The χ-induced fields, $\mathrm{B_x}$ and $\mathrm{B_{ICBM}}$, were computed by applying the SVC to both the estimated susceptibility map $\hat{\chi}$ and χ_{ICBM}, respectively,as shown in Fig 4(d) and (e): (left) the computed χ-induced field (kHz) using χ_{ICBM}; (center) the computed field using $\hat{\chi}$; (right) the difference image. Both χ-maps exhibit typical strong local inhomogeneous field structures caused by the frontal sinus, the sphenoid sinus, the nasal passage, and the

ear canal. These are the critical part of the field map estimation because of the severe geometric distortions in EPI around the air/tissue and air/bone interfaces.

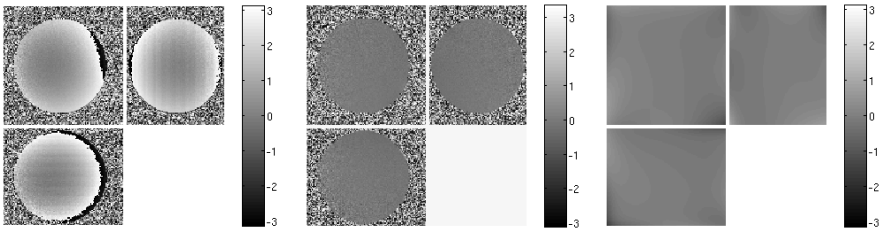

(a) $\angle I_{TE1}$ [rad] of channel #1 (b) Phase difference map $\angle(\bar{I}_{TE1} \cdot I_{TE2})$ [rad] (c) Smoothed phase difference map to be used as $\tilde{\theta}_{\text{sys}}$

Fig. 1. The estimation of the system-specific field component (θ_{sys}) using a homogeneous phantom: (a) the phase of one of the image pair, I_{TE1}, (b) the phase difference map from the image pair which is assumed to be the system-specific component $\theta_{\text{sys}} = \angle(\bar{I}_{TE1} \cdot I_{TE2}) = \gamma \Delta T_E \Delta B_{\text{sys}}$ of the coil channel #1, and (c) the smoothed phase difference map ($\tilde{\theta}_{\text{sys}}$) by the global (3-D) polynomial fitting.

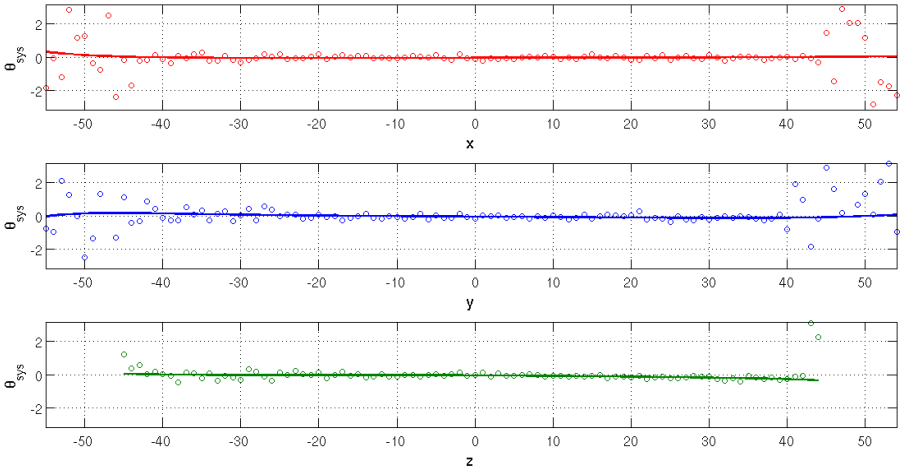

Fig. 2. Middle cross sections comparing the phase difference maps from the homogeneous phantom data (circles) and the smoothed phase difference map by the global polynomial fitting (solid lines)

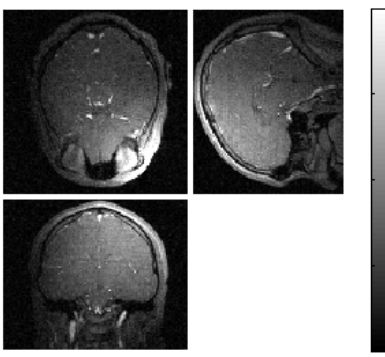

(a) $|I_{TE1}|$ of channel #1

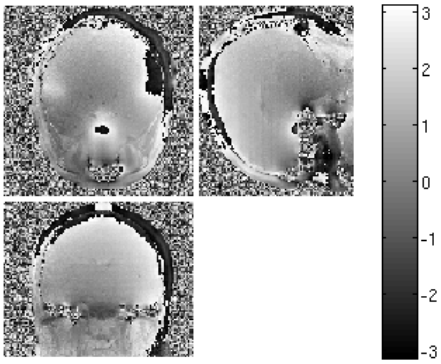

(b) $\angle I_{TE1}$ [rad] of channel #1

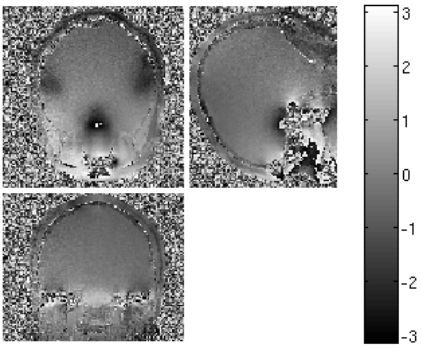

(c) Phase difference map
$\angle(\bar{I}_{TE1} \cdot I_{TE2}) - \tilde{\theta}_{\text{sys}}$ [rad]

Fig. 3. Human brain data: (a) the magnitude and (b) phase images, I_{TE1}, (c) the phase difference map from the image pair I_{TE1} and I_{TE2}, after the system-specific component $\tilde{\theta}_{\text{sys}}$, estimated using the homogeneous phantom, was subtracted

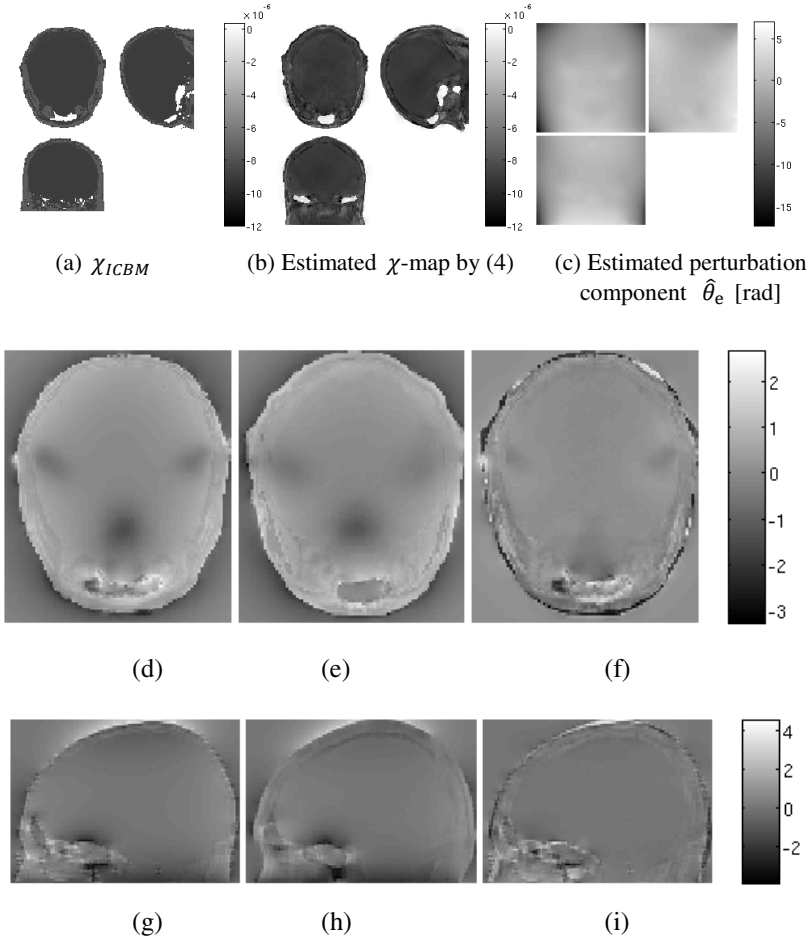

Fig. 4. The estimated susceptibility map: (a) χ-map generated by filling the literature values in the registered ICBM image on to I_{TE1}, (b) the estimated χ-map by (4), (c) the estimated perturbation error component $\hat{\theta}_e$ by (4). Comparisons of the computed χ-induced field maps (kHz) at the middle transverse (top) and sagittal (bottom) planes. (d, g) The χ-map generated from ICBM and (e, h) estimated from the static field map, and (f, i) the difference image.

4 Conclusion and Future Works

The proposed method estimates a susceptibility-induced field map from a measured static field map. It does not require segmentation or pulse sequence modifications, and may yield dynamic field maps that address nonlinear changes due to head rotations. We introduced an effective probability density function of the non-uniform

noise in the phase difference images and investigated a method to empirically meas ure non-χ-induced field inhomogeneities and characterized their magnitudes. The experiments presented showed that the proposed estimator provided a reasonable estimate of the susceptibility-map by successfully separating the susceptibility-induced field ΔB_{x} and the perturbation error field component ΔB_{e}. The χ -induced field map estimate from the human brain was close to the theoretical field map computed from using the brain atlas. Possible sources of error may be the registration error between the human data and the ICBM brain atlas. The effects of non-χ-induced field inhomogeneities, i.e., ΔB_{sys} and ΔB_{e}, in image distortion and reconstruction along with the motion induced χ-induced field changes need to be assessed for the use of the estimated χ-map in time series data reconstruction.

References

1. Edelman, R.R., Wielopolski, P., Schmitt, F.: Echo-Planar MR Imaging. Radiology 192(3), 600–612 (1994)
2. Jezzard, P., Balaban, R.S.: Correction for Geometric Distortion in Echo Planar Images from B0 Field Variations. Magnetic Resonance in Medicine 34, 65–73 (1995)
3. Zeng, H., Constable, R.T.: Image Distotion Correction in EPI: Comparison of Field Mapping With Point Spread Function Mapping. Magnetic Resonance in Medicine 48, 137–146 (2002)
4. Hsu, Y., Han, C., Tseng, W.I.: Correction for Susceptibility-Induced Distrotion in Echo-Planar Imaging Using Field Maps and Model-Based Point Spread Function. IEEE Transactions on Medical Imaging 28(11), 1850–1857 (2009)
5. Yeo, D.T.B., Fessler, J.A., Kim, B.: Motion Robust Magnetic Susceptibility and Field Inhomogeneity Estimation Using Regularized Image Restoration Techniques for fMRI. In: Metaxas, D., Axel, L., Fichtinger, G., Székely, G. (eds.) MICCAI 2008, Part I. LNCS, vol. 5241, pp. 991–998. Springer, Heidelberg (2008)
6. Kim, B., Yeo, D.T.B., Bhagalia, R.: Comprehensive Mathematical Simulation of Functional Magnetic Resonance Imaging Time Series Including Motion-Related Image Distortion and Spin Saturation Effect. Magnetic 26, 147–159 (2008)
7. Viola, P., Wells III, W.M.: Alignment by Maximization of Mutual Information. International Journal of Computer Vision 24(2), 137–154 (1997)
8. Pluim, J.P.W., Maintz, J.B.A., Viergever, M.A.: Mutual-Information-Based Registration of Medical Images: A Survey. IEEE Transactions on Medical Imaging 22(8), 986–1004 (2003)
9. Poynton, C., Jenkinson, M., Whalen, S., Golby, A.J., Wells III, W.: Fieldmap-Free Retrospective Registration and Distortion Correction for EPI-Based Functional Imaging. In: Metaxas, D., Axel, L., Fichtinger, G., Székely, G. (eds.) MICCAI 2008, Part II. LNCS, vol. 5242, pp. 271–279. Springer, Heidelberg (2008)
10. Salomir, R., de Senneville, B.D., Moonen, C.T.: A Fast Calculation Method for Magnetic Field Inhomogeneity due to an Arbitrary Distribution of Bulk Susceptibility. Concepts in Magnetic Resonance Part B: Magnetic Resonance Engineering 19B(1), 26–34 (2003)
11. Yoder, D.A., Zhao, Y., Paschal, C.B., Fitzpatrick, J.M.: MRI Simulator with Object-Specific Field Map Calculations. Magnetic Resonance Imaging 22, 315–328 (2004)

12. Weisskoff, R.M., Kiihne, S.: MRI Susceptometry: Image-Based Measurement of Absolute Susceptibility of MR Contrast Agents and Human Blood. Magnetic Resonance in Medicine 24, 375–383 (1992)
13. Beuf, O., Briguet, A., Lissac, M., Davis, R.: Magnetic Resonance Imaging for the Determination of Magnetic Susceptibility of Materials. Journal of Magnetic Resonance B-112(0120), 111–118 (1996)
14. Wang, Z.J., Li, S., Haselgrove, J.C.: Magnetic Resonance Imaging Measurement of Volume Magnetic Susceptibility Using a Boundary Condition. Journal of Magnetic Resonance 140, 477–481 (1999)
15. Liu, T., Spincemaille, P., de Rochefort, L., Kressler, B., Wang, Y.: Calculation of Susceptibility Through Multiple Orientation Sampling (COSMOS): A Method for Conditioning the Inverse Problem from Measured Magnetic Field Map to Susceptibility Source Image in MRI. Magnetic Resonance in Medicine 61, 196–204 (2009)
16. Schafer, A., Wharton, S., Bowtell, R.: Calculation of Susceptibility Maps from Phase Image Data. In: Proceedings of International Society for Magnetic Resonance in Medicine, vol. 16 (2008)
17. Morgan, J., Irarrazaval, P.: Efficient Solving for Arbitrary Susceptibility Distributions using Residual Difference Fields. In: Proceedings of International Society for Magnetic Resonance in Medicine, vol. 15 (2007)
18. Kressler, B., De Rochefort, L., Liu, T., Spincemaille, P., Jiang, Q., Wang, Y.: Nonlinear Regularization for Per Voxel Estimation of Magnetic Susceptibility Distributions from MRI Field Maps. IEEE Transactions on Medical Imaging 39(2), 273–281 (2010)
19. de Rochefort, L., Liu, T., Kressler, B., Liu, J., Spincemaille, P.: Quantitative Susceptibility Map Reconstruction from MR Phase Data Using Bayesian Regularization: Validation and Application to Brain Imaging. Magnetic Resonance in Medicine 63, 194–206 (2010)
20. Wharton, S., Bowtell, R.: Whole-Brain Susceptibility Mapping at High Field: A Comparision of Multiple- and Single-Orientation Methods. NeuroImage 53, 515–525 (2010)
21. Liu, T., Liu, J., De Rochefort, L., Spincemaille, P., Khalidov, L., Robert Ledoux, J., Wang, Y.: Morphology Enabled Dipole Inversion (MEDI) from a Single-Angle Acquisition: Comparison with COSMOS in Human Brain Imaging. Magnetic Resonance in Medicine 66, 777–783 (2011)
22. Liu, T., Spincemaille, P., De Rochefort, L., Wong, R., Prince, M., Wang, Y.: Unambiguous Identification of Superparamagnetic Iron Oxide Particles through Quantitative Susceptibility Mapping of the Nonlinear Response to Magnetic Fields. Magnetic REsonance Imaging 28, 1383–1389 (2010)
23. Grabner, G., Trattnig, S., Barth, M.: Filtered Deconvolution of a Simulated and an In Vivo Phase Model of the Human Brain. Journal of Magnetic Resonance Imaging 32, 289–297 (2010)
24. Liu, T., Wisnieff, C., Lou, M., Chen, W., Spincemaille, P., Wang, Y.: Nonlinear Formulation of the Magnetic Field to Source Relationship for Robust Quantitative Susceptibility Mapping. Magnetic Resonance in Medicine (2012)
25. Tang, J., Neelavalli, J., Cheng, Y.N., Buch, S., Haacke, E.M.: Improving Susceptibility Mapping using a Threshold-Based K-space/Image Domain Iterative Reconstruction Approach. Magnetic REsonance in Medicine (2012)
26. Liu, T., Xu, W., Spincemaille, P., Avestimehr, A.S., Wang, Y.: Accuracy of the Morphology Enabled Dipole Inversion (MEDI) Algorithm for Quantitative Susceptibility Mapping in MRI. IEEE Transactions on Medical Imaging 31(3), 816–824 (2012)
27. Wu, B., Li, W., Guidon, A., Liu, C.: Whole Brain Susceptibility Mapping Using Compressed Sensing. Magnetic Resonance in Medicine 67, 137–147 (2012)

28. Liang, Z.-P., Lauterbur, P.C.: Principles of Magnetic Resonance Imaging: A Signal Processing Perspective. Wiley-IEEE Press, Piscataway, NJ (1999)
29. Jenkinson, M., Wilson, J.L., Jezzard, P.: Perturbation Method for Magnetic Field Calculations of Nonconductive Objects. Magnetic Resonance in Medicine 52, 471–477 (2004)
30. Lee, J., Hoppel, K.W., Mango, S.A., Miller, A.R.: Intensity and Phase Statistics of Multilook Polarimetric and Interferometric SAR Imagery. IEEE Transactions on Geoscience and Remote Sensing 32(5), 1017–1028 (1994)
31. Ho, K., Kahn, J.: Exact Probability Density Function for Phase Mesaturement Interferometry. Journal of the Optical Society of America 12, 1984–1989 (1995)
32. Leitao, J.M.N., Figueiredo, M.A.T.: Absolute Phase Image Reconstruction: A Stochastic Nonlinear Filtering Approach. IEEE Transactions on Image Processing 7(6), 868–882 (1998)
33. Goldstein, R.M., Zebken, H.A., Werner, C.L.: Satellite Rader Interferometry: Two-Dimensional Phase Unwrapping. Radio Science 23(4), 713–720 (1988)
34. Chiglia, D.C., Pritt, M.D.: Two-Diumensional Phase Unwrapping: Theory, Algorithms and Software. Wiley-Interscience, New York (1998)
35. Bagher-Ebadian, H., Jiang, Q., Ewing, J.R.: A Modified Fourier Based Phase Unwrapping Algorithm with an Application to MRI venography. Journal of Magnetic Resonance Imaging 27(3), 649–652 (2008)
36. Dias, J.B., Leitao, J.N.: The ZpiM algorithm: A Method for Interferometric Image Reconstruction in SAR/SAS. IEEE Transactions on Image Processing 11(4), 408–422 (2002)
37. Abdul-Rahman, H.S., Gdeisat, M.A., Burton, D.R., Lalor, M.J., Lilley, F., Moore, C.J.: Fast and Robust Three-Dimensional Best Path Phase Unwrapping Algorithm. Applied Optics 46(26), 6623–6635 (2007)
38. Jenkinson, M.: Fast, Automated, N-Dimensional Phase-Unwrapping Algorithm. Magnetic Resonance in Medicine 49, 193–197 (2003)
39. Volkov, V.V., Zhu, Y.: Deterministic Phase Unwrapping in the Presence of Noise. Optics Letters 28(22), 2156–2158 (2003)
40. Truong, T., Clymer, B.D., Chakeres, D.W., Schmalbrock, P.: Three-Dimensional Numerical Simulations of Susceptibility-Induced Magnetic Field Inhomogeneities in the Human Head. Magnetic Resonance Imaging 20, 759–770 (2002)
41. Wharton, S., Schafer, A., Bowtell, R.: Susceptibility Mapping in the Human Brain Using Threshold-Based k-Space Division. Magnetic Resonance in Medicine 63, 1292–1304 (2010)
42. Roemer, P.B., Edelstein, W.A., Hayes, C.E., Souza, S.P., Mueller, O.M.: The NMR Phase Array. Magnetic Resonance in Medicine 16, 192–225 (1990)
43. Horowitz, J.L.: Semiparametric and Nonparametric Methods in Econometrics. Springer Series in Statistics. Springer, Evanston (2009)
44. Holmes, C.J., Hoge, R., Collins, L., Woods, R., Toga, A.W., Evans, A.C.: Enhancement of MR Images using Registration for Signal Averaging. Journal of Computer Assisted Tomography 22(2), 324–333 (1998)
45. Schenck, J.F.: The Role of Magnetic Susceptibility in Magnetic Resonance Imaging: MRI Magnetic Compatibility of the First and Second Kinds. Medical Physics 23(6), 815–850 (1996)

Appendix

*A*ssuming that both images I_{TE1} and I_{TE2} carry *i.i.d.* complex white Gaussian noise ϵ with standard deviation σ, they can be expressed as

$$I_{TE1}(\mathbf{r}) = f(\mathbf{r}) + \varepsilon_1(\mathbf{r})$$
$$I_{TE2}(\mathbf{r}) = a(\mathbf{r})f(\mathbf{r})e^{j\theta(\mathbf{r})} + \varepsilon_2(\mathbf{r})$$

where $f(\mathbf{r})$ is the noise free complex-valued image of I_{TE1}, $a(\mathbf{r})$ is the intensity scaling (real-valued) function due to the free induction decay from T_{E1} to T_{E2}, $\theta(\mathbf{r})$ is the phase difference map between I_{TE1} and I_{TE2}, and $\varepsilon_1(\mathbf{r})$ and $\varepsilon_2(\mathbf{r})$ are noise, i.e. $\varepsilon_1, \varepsilon_2 \sim \mathcal{CN}(0, \sigma^2)$. Then, we can express the product of I_{TE2} and the complex conjugate of I_{TE1} as g:

$$\begin{aligned} g(\mathbf{r}) &= \bar{I}_{TE1}(\mathbf{r}) \cdot I_{TE2}(\mathbf{r}) \\ &= a|f|^2 e^{j\theta} + |f|^2 \left(\frac{af}{\bar{f}} e^{j\theta} \bar{\varepsilon}_1 + \frac{\bar{f}}{f} \varepsilon_2 \right) + \bar{\varepsilon}_1 \varepsilon_2 \\ &= a(\mathbf{r})|f(\mathbf{r})|^2 e^{j\theta} + \epsilon(\mathbf{r}). \end{aligned}$$

where the variance ς^2 of ϵ is voxel intensity dependent:

$$\varsigma^2(\mathbf{r}) = \mathrm{var}\{\epsilon(\mathbf{r})\} = |f|^2(1 + a^2)\sigma^2 + \sigma^4.$$

When $|f|^2 \ll \sigma^2$, the noise ϵ can be assumed to be Gaussian (Note: strictly speaking, it is a mixture of Gaussian and normal product distribution), we approximately express the PDF of ϵ as

$$\begin{aligned} p(\epsilon) &= p(\Re\{\epsilon\}, \Im\{\epsilon\}) \\ &\approx \frac{1}{2\pi\varsigma^2} \exp\left[-\frac{1}{2\varsigma^2} (\Re\{g\} - a|f|^2 \cos\theta)^2 - \frac{1}{2\varsigma^2} (\Im\{g\} - a|f|^2 \sin\theta)^2 \right] \\ &= \frac{1}{2\pi\varsigma^2} \exp\left[-\frac{1}{2\varsigma^2} \{|g|^2 + a^2|f|^4 - 2a|f|^2|g| \cos(\theta - \angle g)\} \right] \\ &= \frac{1}{2\pi\varsigma^2} \exp\left[-\frac{|g|^2 + a^2|f|^4}{2\varsigma^2} \right] \cdot \exp\left[\underbrace{\frac{a|f|^2|g|}{\varsigma^2}}_{\kappa} \cos \underbrace{(\theta - \angle g)}_{\eta} \right]. \end{aligned}$$

Therefore, for small σ^2, we have the approximated PDF of η as

$$p\big(\eta(\mathbf{r})\big) \propto \exp\big\{\kappa(\mathbf{r}) \cdot \cos\eta(\mathbf{r})\big\} \quad \text{with} \quad \kappa(\mathbf{r}) \approx \frac{|I_{TE1}(\mathbf{r})|^2 |I_{TE2}(\mathbf{r})|^2}{(|I_{TE1}(\mathbf{r})|^2 + |I_{TE2}(\mathbf{r})|^2)\sigma^2 + \sigma^4}.$$